crystals

MDPI

Article

Segregation of Phosphorus and Silicon at the Grain Boundary in Bcc Iron via Machine-Learned Force Fields

Miroslav Černý [1,2,*] and Petr Šesták [1,2]

[1] Central European Institute of Technology, Brno University of Technology (CEITEC BUT), Purkyňova 123, 612 69 Brno, Czech Republic; sestak@fme.vutbr.cz
[2] Faculty of Mechanical Engineering, Brno University of Technology, Technická 2896/2, 616 69 Brno, Czech Republic
* Correspondence: mcerny@vutbr.cz; Tel.: +420-541-142-709

Abstract: The study of the effects of impurity on grain boundaries is a critical aspect of materials science, particularly when it comes to understanding and controlling the properties of materials for specific applications. One of the related key issues is the segregation preference of impurity atoms in the grain boundary region. In this paper, we employed the on-the-fly machine learning to generate force fields, which were subsequently used to calculate the segregation energies of phosphorus and silicon in bcc iron containing the ∑5(310)[001] grain boundary. The generated force fields were successfully benchmarked using ab initio data. Our further calculations considered impurity atoms at a number of possible interstitial and substitutional segregation sites. Our predictions of the preferred sites agree with the experimental observations. Planar concentration of impurity atoms affects the segregation energy and, moreover, can change the preferred segregation sites.

Keywords: DFT calculations; machine learning; grain boundaries; impurity segregation

check for updates

Citation: Černý, M.; Šesták, P. Segregation of Phosphorus and Silicon at the Grain Boundary in Bcc Iron via Machine-Learned Force Fields. *Crystals* **2024**, *14*, 74. https://doi.org/10.3390/cryst14010074

Academic Editor: Vladislav V. Kharton

Received: 21 December 2023
Revised: 5 January 2024
Accepted: 9 January 2024
Published: 12 January 2024

1. Introduction

The polycrystalline materials used in the majority of technological applications are composed of many smaller or larger grains, each having its own crystallographic orientation. Grain boundaries (GBs), the interfaces that exist between individual grains, represent planar lattice defects critical in determining the properties and behavior of polycrystalline materials [1,2]. GBs can act as obstacles to the motion of dislocations, impacting the material's strength and ductility. They can also form the weakest regions of the crystal, leading to intergranular fracture. Their effect can be seen not only in a reduced cohesion due to different coordination of atoms and often locally reduced density, but also in different chemical composition because impurities tend to segregate preferentially to grain boundaries [3–5].

Impurities can affect the mechanical properties of grain boundaries. For example, the presence of certain elements may lead to embrittlement of the grain boundaries, making the material more prone to fracture [6–8]. Therefore, studies of grain boundaries and the effect of impurity segregation are essential in the field of materials science and engineering, and much effort has been devoted to both experimental and theoretical research in this field. Theoretical methods often aim to calculate the cohesive (cleavage energy) or tensile strength of GB to estimate the effect of segregated impurities on the mechanical response of polycrystals. Although reduced cohesion of grains due to impurities segregated to the GB has been reported in numerous papers, it is not the only mechanism of intergranular embrittlement. For example, Ko et al. [9] reported for the case of phosphorus in iron that the governing mechanism of the intergranular embrittlement is inhibition of nucleation of dislocations near the crack rather than the conventional reasoning that focuses on the GB decohesion. However, regardless of the embrittling mechanism, correct prediction of preferential segregation sites remains a crucial issue. Some of the theoretical predictions

are in conflict with experimental observations (see, e.g., the discussion in Ref. [10]). There are several explanations for such a disagreement. Some of them are based on the effect of entropy terms [10] at elevated temperatures, which are often neglected in atomistic calculations, and only few studies considering the entropy have been published so far [11–14]. Another explanation is based on the limited size of computational cells [15].

Among the theoretical methods used for periodic systems, metallic ones in particular, ab initio calculations employing the density functional theory (DFT) belong to those most accurate. Unfortunately, they have certain limitations that arise from their high computational demands. The most serious limitation is the limited size of simulation cells, which sometimes leads to unrealistic concentrations of impurities or a limited amount of degrees of freedom. Calculations based on empirical or semi-empirical interatomic potentials are computationally much cheaper, but often at the price of reduced accuracy and reliability. A certain way to greatly reduce computational cost but without the need to sacrifice the accuracy is the application of force fields generated by machine learning. Prediction of desired property is performed automatically by interpolations between known training systems that were previously calculated from first principles [16]. An automatic way to pick ab initio data and add them to the training set is the on-the-fly learning during the run of the ab initio molecular dynamics simulation. Recent studies of grain boundaries using machine learning approaches [13,17–19] reported results very encouraging for wider applications of these methods.

The aim of this paper is to employ machine-learned force fields for calculations of segregation energy in computational cells, which are large enough to also address the effect of impurity concentration on the predicted segregation sites. We focus on two impurity atoms, phosphorus and silicon, in bcc iron that contains the symmetric $\sum$5(310)[001] tilt grain boundary, where the $\sum$ value represents the volume of the coincident site lattice (CSL) of the grain boundary in terms of the volume of the unit cell of the crystal. The subsequent indices in the round and square brackets are the Miller indices of the GB plane and the shared tilt axis, respectively. For a more detailed explanation, the reader is referred to books such as Sutton and Balluffi [1], Randle [20], or Lejček [2]. The reason for choosing the two aforementioned impurities is the order-of-magnitude different solubility of these two elements in iron (0.033 for P vs. 0.305 for Si [2]), and also the different preference for segregation. While P atoms were experimentally observed to occupy interstitial positions at grain boundaries in Fe, Si was determined to be the substitutional impurity.

2. Materials and Methods

2.1. On-the-Fly Machine Learning Process

The Machine-Learned Force Fields (MLFF) were obtained with the help of the Vienna Ab Initio Simulation Package (VASP) [21,22] (version 6.3.0) via the on-the-fly ab initio molecular dynamics simulations. This code used the projector augmented waves method [23] and the exchange-correlation energy was evaluated within the generalized gradient approximation parametrized by Perdew, Burke, and Ernzerhof (PBE) [24]. The magnetic orderings of Fe atoms were taken into account by means of the spin polarized calculations. The plane-wave cut-off energy was set to 400 eV. The energy converged in the self-consistent cycle to reduce its fluctuations below 1×10^{-6} eV.

The MLFF training was performed on a supercell containing 180 atoms and $\sum$5(310) GB illustrated in Figure 1 with the help of the visualization software VESTA [25]. To effectively describe the impurity interactions with host atoms in a variety of relevant configurations, the supercell was designed to contain impurity atoms located at GBs in both the substitutional and interstitial positions, and two other impurity atoms were located in substitutional positions in the bulk part of the supercell, i.e., approximately in the middle of the grain. Numerical integration in the Brillouin zone was performed using a mesh of *k*-points distributed so that their maximum distance in the reciprocal space was 0.25 Å^{-1}. Therefore, a sampling using the $19 \times 6 \times 2$ Γ-centered Monkhorst-Pack mesh was employed for the aforementioned supercell with the approximate dimensions $8.7 \times 8.9 \times 28.4$ Å.

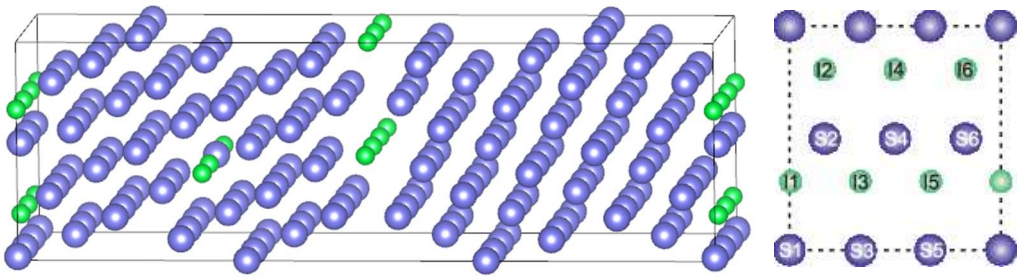

(**a**) (**b**)

Figure 1. (**a**) Illustration of the computational supercell with ∑5(310)[001] GB in the bcc lattice employed for machine learning. Each supercell contains two grain boundaries. The impurity atoms (green spheres) are placed interstitially at one of them and substitutionally at the other one. In addition, two impurity atoms substitute Fe atoms inside the grain. (**b**) A single (310) atomic plane containing six sites for substitutional segregation (S1–S6) and six sites for interstitial segregation (I1–I6).

The way of generating the training set in VASP is the same as described briefly in the introduction and more thoroughly in the references [26,27]. Ab initio molecular dynamics (AIMD) simulations served as a tool for generating atomic configurations, which formed the source for the structure dataset, relevant to the considered model of GB. In the first stage, the system was heated to 500 K in 5000 steps with an isothermal–isobaric (NpT) ensemble using the Langevin thermostat. After that, the training process continued with another 5000 steps at a constant temperature of 500 K. The AIMD time step was set to 2 fs. During both stages, the procedure implemented in the VASP code automatically makes decisions, based on the uncertainty in the prediction of the energy, forces, and stresses and the history of previous sampling, if the first-principles calculation must be performed or can be skipped. Such a learning process reduces the need for human interventions. The cutoff radius for the radial descriptor was set to 7 Å, while the cutoff radius for the angular descriptor kept the default value of 5 Å.

2.2. Benchmarking

To verify the reliability of generated MLFF, we conducted a very simple comparison of the computed data with the DFT results. To make the benchmark less time-consuming (particularly for DFT calculations), we used a smaller supercell with 60 atoms, which is illustrated in Figure 2. The coordination system was oriented so that the x-, y-, and z-axes were parallel to the crystallographic directions [001], $[1\bar{3}0]$, and [310], respectively. First, we created a clean supercell with the ∑5(310)[001] GB and used the VASP code to optimize the atomic positions and the length of the supercell (measured along the [310] direction, which is perpendicular to the GBs). The forces acting on atoms were relaxed to be less than 1×10^{-3} eV/Å and the stress was minimized to be less than 0.01 Gpa. The optimized supercell had dimensions of $2.83 \times 8.96 \times 27.47$ Å. Next, we introduced impurity atoms to several inequivalent positions in the optimized supercell and computed the energy without any further relaxation. The positions are numbered according to the atomic planes, as can be seen in Figure 2. Since the supercell has 2 atoms per plane, each grain contains 15 atomic planes. Therefore, the substitutional positions are numbered 1–8 and the positions for interstitial impurities (smaller circles) are labeled as 0. We introduced two impurity atoms (to occupy both available positions) to both grains (to equivalent planes) at the time. If the impurity atoms occupy interstitial positions, the supercell contains 60 Fe atoms and 4 atoms of the impurity. In the case of substitutional segregation, the cell contains 56 Fe atoms and 4 impurity atoms.

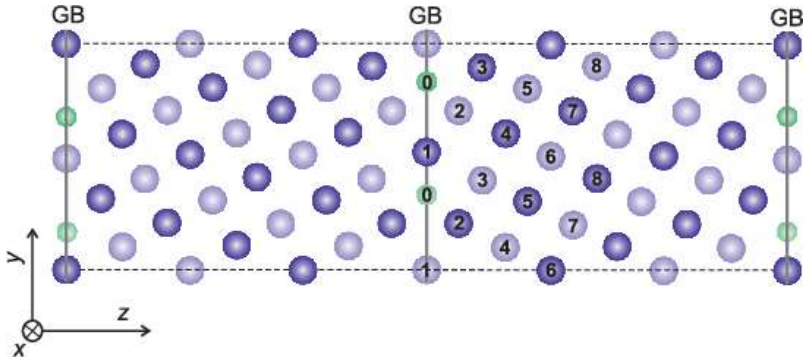

Figure 2. The computational supercell with ∑5(310) GB for benchmarking. Darker and lighter spheres represent atoms in the front and the next (001) plane, the green spheres show the interstitial positions. Numbering of the atomic planes is indicated only for selected atoms (the others are symmetrically equivalent because of the mirror symmetry of the computational cell.

Subsequently, we used the MLFF to calculate the energy of the same supercells, which were employed for the DFT benchmarking (again, without any relaxation). Since the main goal of the generated MLFF is to study the segregation of impurities at the GB, we calculated the difference between the total energy E_i of a supercell with the impurity in the plane I and the energy E_8 of a supercell with impurity in the plane 8. Although these energy differences are not equal to the segregation energy, they can serve as a simple indicator of the accuracy of MLFF.

The results of the benchmarking are shown in Figure 3. The agreement of DFT and MLFF data is very satisfactory, which encourages us to employ the generated MLFF in further calculations of the segregation energy. On the other hand, it is surprising that both elements exhibit $E_i - E_8$ profiles, which indicate a preference for segregation in interstitial positions at the GB. This is in contradiction with the experimental data for the segregation of Si in Fe.

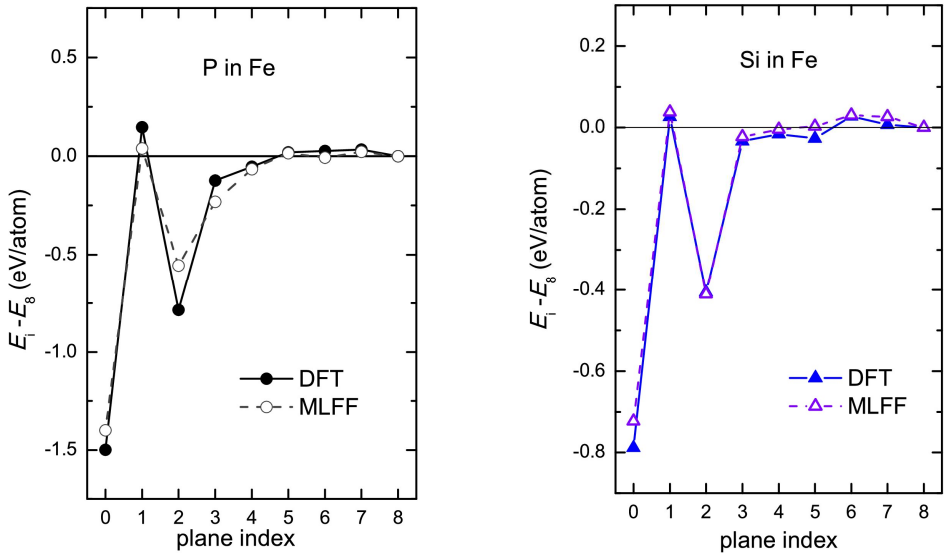

Figure 3. The energy difference $E_i - E_8$ computed for (**a**) phosphorus and (**b**) silicon in the bcc crystal of Fe with the ∑5 GB. The results were calculated using the generated MLFF (dashed lines) and using the DFT (the solid lines).

2.3. Calculations of Segregation Energy

Since we focus on the ∑5(310) GB, all computational supercells considered in the present calculations are built as multiples of a certain minimum repetitive cell. To obey

the periodic boundary conditions, the length of the supercell (measured along the *z*-axis in Figure 2) is given by the number units based on the so-called coincident site lattice. The transverse dimensions must be multiples of the minimum widths of the cell in Figure 2. Therefore, we denote the cell for benchmarking as the $1 \times 1 \times 3$ supercell and the cell used for machine learning (Figure 1) is referred to as the $3 \times 1 \times 3$ supercell.

The lengths of the computational supercells (measured along the [310] direction) were optimized to reduce the corresponding stress tensor component σ_3 below 0.09 GPa. The transverse lattice parameters were kept constant and equal to those of the bulk crystal. This avoids errors related to interfacial stress and the resulting elastic energy stored in the simulated grain [28]. The residual forces acting on the atoms were relaxed to be less than 1×10^{-3} eV/Å. The segregation energy E_s was calculated according to the formula

$$E_s = (E_{GB,i} - E_{GB})/N - (E_{b,i} - E_b),$$

where N represents the number of impurity atoms in the supercell and $E_{GB,i}$ and E_{GB} are energies of the computational supercell containing ∑5(310) GB with and without impurity atoms, respectively. Similarly, $E_{b,i}$, and E_b represent the energies of impurity-containing and clean bulk supercells. In the case of interstitial segregation, the value of $E_{GB,i}$ was reduced by subtracting the energy of N iron atoms in the bulk configuration. The energy calculations for the bulk were performed on cubic supercells (containing only one impurity atom), which were obtained as $n \times n \times n$ multiples of the conventional cubic cell. The computed differences $E_{b,i} - E_b$ were calculated for supercells of different sizes and a good convergence (within 1.5 meV) was found for $n = 4$ and above.

3. Results

3.1. Ground-State Properties

To further verify the reliability of the generated MLFF, we used them to calculate the energy–volume curves for a bulk bcc Fe crystal and determined the equilibrium lattice parameter a_0 and the bulk modulus B. Next, we relaxed supercells containing ∑5(310) GB without any impurity and calculated their interfacial energy. The values obtained using MLFF that were generated for both the P and Si atoms introduced as impurities in the Fe matrix are compared with the data from the literature in Table 1. While the benchmark in Section 2.2 primarily tested the precision of the impurity-Fe interactions, the values in Table 1 can serve as an indication of the reliability of the interactions between Fe atoms in both MLFF.

It is evident that the computed values of a_0 and B are in good agreement with the experimental results and the GB energy is consistent with the values previously reported in the literature. All the values listed in Table 1 were computed using DFT approaches in models of a clean bulk iron or clean grain boundaries. Compared to values calculated using semiempirical interatomic potentials (0.99 J·m^{-2} [29], 1.11 J·m^{-2} [30]) or with the help of the atomic density function (1.49 J·m^{-2} [31]), our MLFF results appear to be much closer to the ab initio level of accuracy.

Table 1. Values of the equilibrium lattice parameter a_0, the bulk modulus B of a clean bulk crystal of bcc Fe, and the grain boundary energy γ_{GB}, calculated using the MLFF generated for Fe + Si and Fe + P together with available experimental or literature data for a clean Fe.

Property	ML_{Fe+P}	ML_{Fe+Si}	Literature
a_0 (Å)	2.838	2.830	2.83 [32], 2.87 [33], 2.85 [34], 2.87 [35] [e]
B (GPa)	158	177	190 [32], 178 [33], 186 [34], 168 [35] [e]
γ_{GB} (J·m^{-2})	1.56	1.57	1.53 [36], 1.56 [14], 1.55 [37], 1.57 [38]

[e] Experimental data.

3.2. Supercell Size Effect

First, we searched for the optimum size of the computational cell. One of the most critical points in atomistic studies of impurity segregation is the reliability of the calculated segregation energies for low concentrations of impurity atoms. Small computational cells employed within periodic boundary conditions always lead to a high planar concentration of impurities, or, in other words, to small distances between impurity atoms that strongly interact with each other. On the other hand, when their distance becomes sufficiently large, their interactions become negligible, and a further increase in the computational cell size does not lead to significant changes in the segregation energy.

The results of our optimization tests are presented in Figure 4 for the example of a single P atom in a number of substitutional positions. The computational cells were constructed as $m \times n \times o$ supercells with a subsequently relaxed stress σ_3 and optimized atomic positions. It is evident that, starting from plane 5, the E_{seg} values computed for P become constant. Thus, the GB region spans from the GB plane through the first five neighboring planes. The segregation profiles for Si (not plotted here) indicated a very similar span of the GB region. Since these results were obtained in relaxed supercells with different concentrations of impurities, all the $E_i - E_{13}$ values presented differ from those shown in Figure 3. One can see that the thinnest supercells ($1 \times 1 \times 3$ and $1 \times 1 \times 5$) predict energy values very different from those of the other cells. These cells contain only two atoms per (310) plane, so replacing one of them with the impurity atom leads to a planar impurity concentration of 0.5. Although the difference between profiles computed for these supercells differ only slightly, all other supercells considered were constructed longer along the z axis to include a sufficiently large bulk region, separating the grain boundaries. Starting from the $2 \times 1 \times 5$ supercell, the $E_i - E_{13}$ values seem to converge very well and the energies computed in the $3 \times 1 \times 5$ supercell differ from those computed in the $6 \times 2 \times 5$ supercell by less than 0.015 eV. Therefore, the supercell used for further calculations of the segregation energy E_s was constructed as a $3 \times 1 \times 5$ supercell, representing a good compromise between computational demands and accuracy.

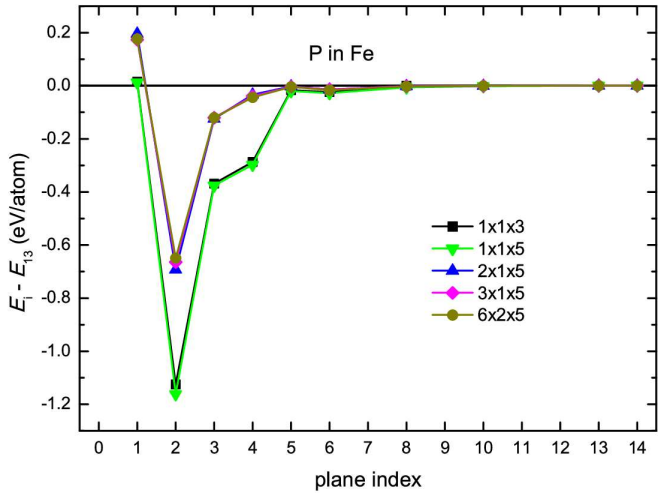

Figure 4. The values of the energy difference $E_i - E_{13}$ computed using the generated MLFF for a single phosphorus atom substituting Fe atom in the atomic plane i.

3.3. Segregation Energy

Even if the solubility of impurity atoms in the host metal is low, their local concentration near the grain boundary can be increased significantly. For this reason, we also considered the effect of the planar concentration of the impurity atoms on their segregation preference. Since the computational cell used for these calculations was constructed as the $3 \times 1 \times 5$ supercell, it contains six atoms in each plane (see Figure 1b) that allow

N = 1–6 impurity atoms to substitute the host (Fe) atoms. Similarly, the GB plane offers six interstitial positions for segregation of impurity atoms.

Naturally, the distribution of impurity atoms in the computational cell plays an important role. Here, we limit our attention to single-plane segregation. All the impurity atoms are in one plane, but, depending on the planar concentration, there are several possible distributions. While there is no need for more than a single calculation for supercells with 1, 5, or 6 impurity atoms since for N = 6 there is only one possible configuration and for N = 1 and N = 5 all possible configurations are equivalent, we must consider three configurations for N = 2, 3, and 4. That is, for N = 2, we studied substitutional impurities in positions S1 + S2, S1 + S3, and S1 + S4 labeled in Figure 1b. All the other possible configurations would be symmetrically equivalent. For N = 3, the configurations considered were S1 + S2 + S3, S1 + S2 + S4, and S1 + S3 + S5. For N = 4, we can simply create an inversion of the configurations for two impurity atoms, i.e., we employ the configurations with impurity atoms at sites S3 + S4 + S5 + S6, S2 + S4 + S5 + S6 and S2 + S3 + S5 + S6. The same configurations were considered for the interstitial segregation sites.

Our calculations revealed that phosphorus atoms prefer to be as close to each other as possible and tend to form chains of atoms along the [001] direction. This means that the lowest energy for two, three, and four P atoms is obtained for the arrangements S1 + S3, S1 + S3 + S5 and S2 + S4 + S5 + S6, respectively. It is consistent with the observation that, in relaxed supercells, the P atoms attract each other. For interstitial segregations, we predict the equivalent arrangements I1 + I3, I1 + I3 + I5 and I2 + I4 + I5 + I6 as those most energetically favorable. On the contrary, Si atoms repel each other, which results in their lowest-energy arrangements different from those of P atoms. The Si atoms prefer to occupy the sites S1 + S2, S1 + S2 + S3 and S3 + S4 + S5 + S6 (I1 + I2, I1 + I2 + I3 and I3 + I4 + I5 + I6) for N = 2, N = 3, and N = 4, respectively. The segregation energy values for phosphorus and silicon plotted in Figure 5 were taken as the minimum energy configurations for the particular impurity concentration.

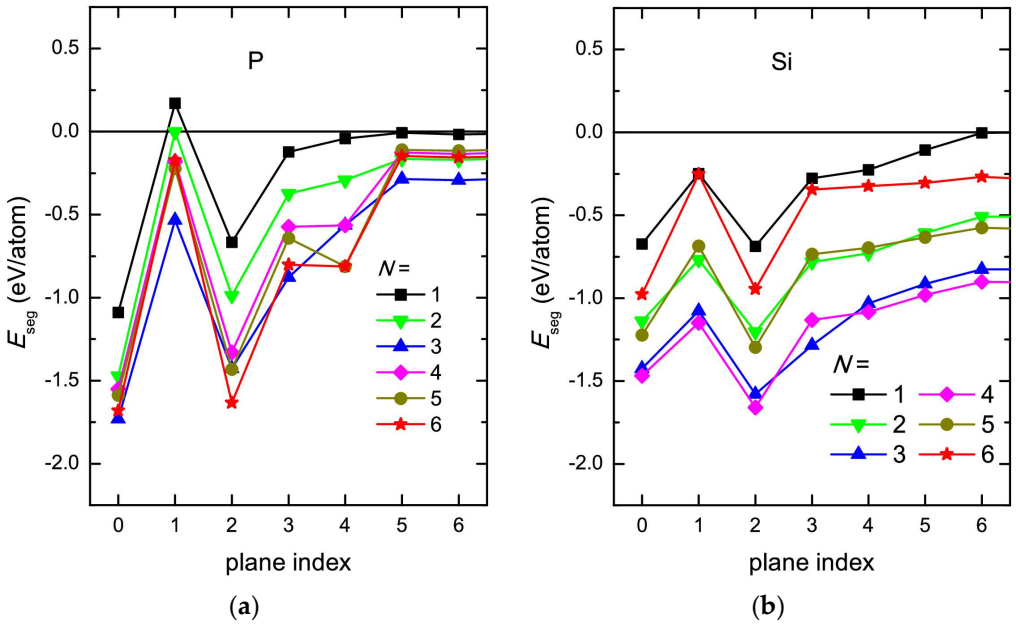

Figure 5. Values of the segregation energy E_{seg} of (**a**) phosphorus and (**b**) silicon computed for six (310) planes (planes 1–6) in the GB region considering different amounts N of impurity atoms. The plane index 0 denotes the values calculated for interstitial positions at the GB plane.

Although the $E_i - E_8$ values are not equal to E_{seg}, the trends are similar. Note that the impurity concentration in the supercell used for the benchmarking is equivalent to N = 6 in Figure 5. For both impurities and all impurity concentrations, we can see competition between interstitial positions and substitutional positions in plane 2, next to the GB plane.

To make the energy differences for these competing segregation sites more visible, we plot the E_{seg} values computed for sites 0 and 2 as functions of the number N of solute (impurity) atoms in the considered plane in Figure 6. The planar solute concentration equals $N/6$.

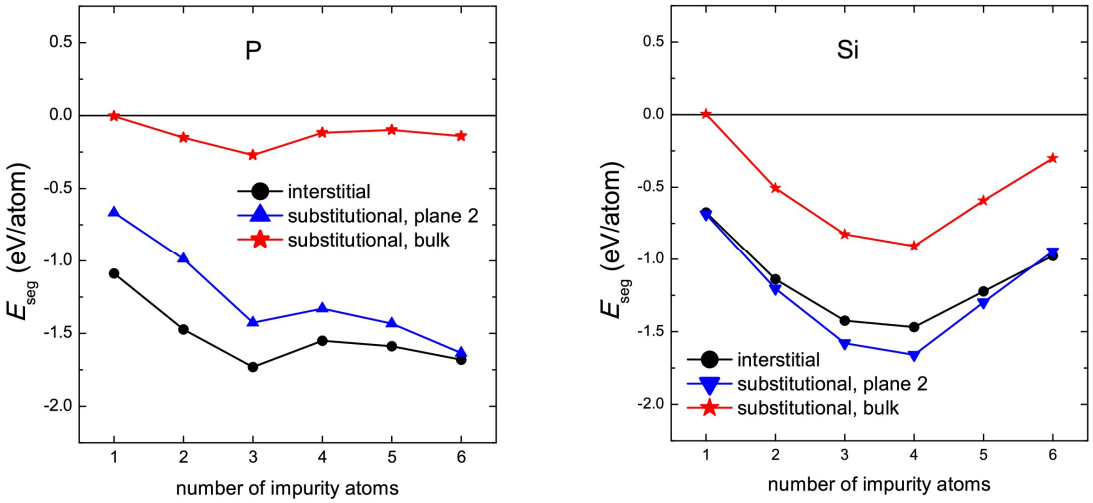

Figure 6. The values of the segregation energy computed for (**a**) phosphorus and (**b**) silicon at interstitial sites and substitutional sites in planes 2 and 13 (the bulk region of the supercell) as a function of the number of impurity atoms in the atomic plane.

When P is an impurity, the preferred segregation sites are interstitial. The energy difference decreases with increasing N and, for the highest impurity concentration, becomes negligible. The differences in the segregation energies of silicon in the interstitial and substitutional positions are even smaller than those calculated for P. Interestingly, they are almost zero for both extreme concentrations with N = 1, and N = 6. Intermediate concentrations predict the substitutional segregation that is energetically favorable. For N = 6, the preferred segregation site turns to interstitial. Although this prediction is based on a very small energy difference, it is consistent with the computed values of $E_i - E_8$ in Figure 3.

4. Discussion

The prediction of the interstitial site as the preferred segregation site of P at ∑5(310) GB in iron is in agreement with experimental observations [2]. Our E_{seg} profile in Figure 5 is in good agreement with recent calculations of the trapping energy by Ebihara and Suzudo [39] based on the embedded atom method. Lejček et al. [10] calculated the binding energy of phosphorus in the interstitial and substitutional sites in the [310] GB plane in bcc Fe as a function of the lattice parameter. Changes in the lattice parameter were applied to imitate the thermal expansion of the lattice. The authors reported for the impurity concentration corresponding to N = 6 that, while the binding energy of P at the substitutional site was predicted to remain almost constant, the values of interstitially segregated P decreased with the increase in the lattice parameter, giving a clear preference for interstitial segregation for the equilibrium lattice parameter in Table 1. This seemingly disagrees with our results in Figures 5 and 6, but we must note that the substitutional sites considered in the paper by Lejček et al. [10] correspond to our plane 1, whereas the energetically most probable substitutional positions found in the present work are located in plane 2.

The segregation energy profile computed for Si is qualitatively similar to that reported by Jin et al. [40]. They constructed a smaller supercell with the same cross section. Note that interstitial positions were neglected in their study and therefore the plane indexes are lower by one compared to the present indexing in Figure 5. The segregation of Si in Fe was also studied by Bhattacharya et al. [41], who considered ∑3(111) and ∑11(332) GBs.

Although their segregation energies cannot be directly compared with the present results, their prediction of a higher energy for two-site segregation than for one-site segregation is consistent with our finding that E_{seg} for $N = 6$ is higher than that for $N = 3$.

The E_{seg} profiles obtained for individual planar impurity concentrations look very similar, but they seem to converge to different values of energy, which correspond to the segregation energies for the bulk. This might seem like nonsense, because the segregation energy in the bulk should be zero. The reason for the nonzero E_{seg} values is the fact that we kept the same configuration of impurities in all atomic planes and the impurity atoms were not fully dissolved. The E_{seg} values then expressed the change in energy caused by mutual impurity interactions, the elastic energy introduced by the local lattice distortion, etc. To make this energy change more visible, we added the values computed for plane 13 (representing the bulk part of the supercell) to Figure 6.

It is evident that the planar concentration of the impurity atoms affects the calculated values of the segregation energy. Although the present results indicate a change in the predicted segregation sites only for silicon and the energy difference between the competing sites is very small, we must keep this effect in mind. The possibility of a different prediction of the segregation sites could be one of the reasons why theoretical predictions sometimes do not agree with experimental observations (see, e.g., the DFT data in Ref. [14] and the experimental data gathered in Ref. [2]).

Author Contributions: Conceptualization, M.Č.; Funding acquisition, M.Č.; Investigation, P.Š. and M.Č.; Methodology, M.Č.; Project administration, M.Č.; Visualization, M.Č.; Writing—original draft, M.Č.; Writing—review and editing, M.Č. and P.Š. All authors have read and agreed to the published version of the manuscript.

Funding: This research was funded by the Czech Science Foundation (Project No. GA-20-08130S).

Data Availability Statement: The data presented in this study are available within the article.

Acknowledgments: Computational resources were provided by the Ministry of Education, Youth and Sports of the Czech Republic under the Projects e-INFRA CZ (ID:90254) at the IT4Innovations National Supercomputing Center.

Conflicts of Interest: The authors declare no conflicts of interest. The funders had no role in the design of the study; in the collection, analyses, or interpretation of data; in the writing of the manuscript; or in the decision to publish the results.

References

1. Sutton, A.P.; Balluffi, R.W. *Interfaces in Crystalline Materials*; Clarendon Press: Oxford, UK, 1995; ISBN 978-0-19-851385-8.
2. Lejček, P. *Grain Boundary Segregation in Metals*; Hull, R., Jagadish, C., Osgood, R.M., Jr., Parisi, J., Wang, Z., Warlimont, H., Eds.; Springer Series in Materials Science; Springer: Heidelberg, Germany; Dordrecht, The Netherlands; London, UK; New York, NY, USA, 2010; ISBN 978-3-642-12504-1.
3. McLean, D. *Grain Boundaries in Metals*; Clarendon Press: Oxford, UK, 1957.
4. Flewitt, P.E.J.; Wild, R.K. *Grain Boundaries, Their Microstructure and Chemistry*; John Wiley and Sons, Ltd.: Chichester, UK, 2001.
5. Lejček, P.; Šob, M.; Paidar, V. Interfacial Segregation and Grain Boundary Embrittlement: An Overview and Critical Assessment of Experimental Data and Calculated Results. *Prog. Mater. Sci.* **2017**, *87*, 83–139. [CrossRef]
6. Yamaguchi, M.; Shiga, M.; Kaburaki, H. Grain Boundary Decohesion by Impurity Segregation in a Nickel-Sulfur System. *Science* **2005**, *307*, 393–397. [CrossRef] [PubMed]
7. Wu, R.; Freeman, A.J.; Olson, G.B. Nature of Phosphorus Embrittlement of the Fe $\Sigma3[1\bar{1}0](111)$ Grain Boundary. *Phys. Rev. B* **1994**, *50*, 75. [CrossRef] [PubMed]
8. Mai, H.L.; Cui, X.-Y.; Scheiber, D.; Romaner, L.; Ringer, S.P. The Segregation of Transition Metals to Iron Grain Boundaries and Their Effects on Cohesion. *Acta Mater.* **2022**, *231*, 117902. [CrossRef]
9. Ko, W.-S.; Jeon, J.B.; Lee, C.-H.; Lee, J.-K.; Lee, B.-J. Intergranular Embrittlement of Iron by Phosphorus Segregation: An Atomistic Simulation. *Modell Simul. Mater. Sci. Eng.* **2013**, *21*, 025012. [CrossRef]
10. Lejček, P.; Hofmann, S.; Všianská, M.; Šob, M. Entropy Matters in Grain Boundary Segregation. *Acta Mater.* **2021**, *206*, 116597. [CrossRef]

11. Schönecker, S.; Li, X.; Johansson, B.; Kwon, S.K.; Vitos, L. Thermal Surface Free Energy and Stress of Iron. *Sci. Rep.* **2015**, *5*, 14860. [CrossRef]
12. Scheiber, D.; Popov, M.N.; Romaner, L. Temperature Dependence of Solute Segregation Energies at W GBs from First Principles. *Scr. Mater.* **2023**, *222*, 115059. [CrossRef]
13. Černý, M.; Šesták, P.; Všianská, M.; Lejček, P. On Agreement of Experimental Data and Calculated Results in Grain Boundary Segregation. *Metals* **2022**, *12*, 1389. [CrossRef]
14. Řehák, P.; Všianská, M.; Černý, M. Role of Vibrational Entropy in Impurity Segregation at Grain Boundaries in Bcc Iron. *Comput. Mater. Sci.* **2023**, *216*, 111858. [CrossRef]
15. Lejček, P.; Šob, M.; Paidar, V.; Vitek, V. Why Calculated Energies of Grain Boundary Segregation Are Unreliable When Segregant Solubility Is Low. *Scr. Mater.* **2013**, *68*, 547–550. [CrossRef]
16. Jinnouchi, R.; Lahnsteiner, J.; Karsai, F.; Kresse, G.; Bokdam, M. Phase Transitions of Hybrid Perovskites Simulated by Machine-Learning Force Fields Trained on the Fly with Bayesian Inference. *Phys. Rev. Lett.* **2019**, *122*, 225701. [CrossRef] [PubMed]
17. Zhu, Q.; Samanta, A.; Li, B.; Rudd, R.E.; Frolov, T. Predicting Phase Behavior of Grain Boundaries with Evolutionary Search and Machine Learning. *Nat. Commun.* **2018**, *9*, 467. [CrossRef] [PubMed]
18. Huber, L.; Hadian, R.; Grabowski, B.; Neugebauer, J. A Machine Learning Approach to Model Solute Grain Boundary Segregation. *Npj Comput. Mater.* **2018**, *4*, 64. [CrossRef]
19. Shiihara, Y.; Kanazawa, R.; Matsunaka, D.; Lobzenko, I.; Tsuru, T.; Kohyama, M.; Mori, H. Artificial Neural Network Molecular Mechanics of Iron Grain Boundaries. *Scr. Mater.* **2022**, *207*, 114268. [CrossRef]
20. Randle, V. *The Role of the Coincidence Site Lattice in Grain Boundary Engineering*; Institute of Materials: Midland, MI, USA, 1996; ISBN 1-86125-006-1.
21. Kresse, G.; Hafner, J. Ab Initio Molecular Dynamics for Open-Shell Transition Metals. *Phys. Rev. B* **1993**, *48*, 13115. [CrossRef]
22. Kresse, G.; Furthmüller, J. Efficient Iterative Schemes for Ab Initio Total-Energy Calculations Using a Plane-Wave Basis Set. *Phys. Rev. B* **1996**, *54*, 11169–11186. [CrossRef]
23. Kresse, G.; Joubert, D. From Ultrasoft Pseudopotentials to the Projector Augmented-Wave Method. *Phys. Rev. B* **1999**, *59*, 1758–1775. [CrossRef]
24. Perdew, J.P.; Burke, K.; Ernzerhof, M. Generalized Gradient Approximation Made Simple. *Phys. Rev. Lett.* **1996**, *77*, 3865–3868. [CrossRef]
25. Momma, K.; Izumi, F. It VESTA: A Three-Dimensional Visualization System for Electronic and Structural Analysis. *J. Appl. Crystallogr.* **2008**, *41*, 653–658. [CrossRef]
26. Jinnouchi, R.; Karsai, F.; Kresse, G. On-the-Fly Machine Learning Force Field Generation: Application to Melting Points. *Phys. Rev. B* **2019**, *100*, 014105. [CrossRef]
27. Jinnouchi, R.; Karsai, F.; Verdi, C.; Asahi, R.; Kresse, G. Descriptors Representing Two- and Three-Body Atomic Distributions and Their Effects on the Accuracy of Machine-Learned Inter-Atomic Potentials. *J. Chem. Phys.* **2020**, *152*, 234102. [CrossRef] [PubMed]
28. Černý, M.; Šesták, P.; Řehák, P.; Všianská, M.; Šob, M. Atomistic Approaches to Cleavage of Interfaces. *Modell Simul. Mater. Sci. Eng.* **2019**, *27*, 035007. [CrossRef]
29. Tschopp, M.A.; Solanki, K.N.; Gao, F.; Sun, X.; Khaleel, M.A.; Horstemeyer, M.F. Probing Grain Boundary Sink Strength at the Nanoscale: Energetics and Length Scales of Vacancy and Interstitial Absorption by Grain Boundaries in α-Fe. *Phys. Rev. B* **2012**, *85*, 064108. [CrossRef]
30. Rajagopalan, M.; Tschopp, M.A.; Solanki, K.N. Grain Boundary Segregation of Interstitial and Substitutional Impurity Atoms in Alpha-Iron. *JOM* **2014**, *66*, 129–138. [CrossRef]
31. Kapikranian, O.; Zapolsky, H.; Domain, C.; Patte, R.; Pareige, C.; Radiguet, B.; Pareige, P. Atomic Structure of Grain Boundaries in Iron Modeled Using the Atomic Density Function. *Phys. Rev. B* **2014**, *89*, 014111. [CrossRef]
32. Černý, M. Elastic Stability of Magnetic Crystals under Isotropic Compression and Tension. *Mater. Sci. Eng. A* **2007**, *462*, 432–435. [CrossRef]
33. Alnemrat, S.; Hooper, J.P.; Vasiliev, I.; Kiefer, B. The Role of Equilibrium Volume and Magnetism on the Stability of Iron Phases at High Pressures. *J. Phys. Condens Matter.* **2014**, *26*, 046001. [CrossRef] [PubMed]
34. Friák, M.; Šob, M. Ab Initio Study of the Bcc-Hcp Transformation in Iron. *Phys. Rev. B* **2008**, *77*, 174117. [CrossRef]
35. Kittel, C. *Introduction to Solid State Physics*, 8th ed.; John Wiley & Sons: Hoboken, New Caledonia, 2005.
36. Du, Y.A.; Ismer, L.; Rogal, J.; Hickel, T.; Neugebauer, J.; Drautz, R. First-Principles Study on the Interaction of H Interstitials with Grain Boundaries in α- and γ-Fe. *Phys. Rev. B* **2011**, *84*, 144121. [CrossRef]
37. Hristova, E.; Janisch, R.; Drautz, R.; Hartmaier, A. Solubility of Carbon in α-Iron under Volumetric Strain and Close to the Σ5(310)[001] Grain Boundary: Comparison of DFT and Empirical Potential Methods. *Comput. Mater. Sci.* **2011**, *50*, 1088–1096. [CrossRef]
38. Wang, J.; Madsen, G.K.H.; Drautz, R. Grain Boundaries in Bcc-Fe: A Density-Functional Theory and Tight-Binding Study. *Modell Simul. Mater. Sci. Eng.* **2018**, *26*, 025008. [CrossRef]
39. Ebihara, K.; Suzudo, T. Molecular Dynamics Study of Phosphorus Migration in Σ3(111) and Σ5(0-13) Grain Boundaries of α-Iron. *Metals* **2022**, *12*, 662. [CrossRef]

40. Jin, H.; Elfimov, I.; Militzer, M. Study of the Interaction of Solutes with Σ5 (013) Tilt Grain Boundaries in Iron Using Density-Functional Theory. *J. Appl. Phys.* **2014**, *115*, 093506. [CrossRef]
41. Bhattacharya, S.K.; Kohyama, M.; Tanaka, S.; Shiihara, Y. Si Segregation at Fe Grain Boundaries Analyzed by Ab Initio Local Energy and Local Stress. *J. Phys. Condens Matter.* **2014**, *26*, 355005. [CrossRef]